

Scalable Mechanistic Neural Networks

Jiale Chen

*Institute of Science and Technology Austria (ISTA)
3400 Klosterneuburg, Austria*

JIALE.CHEN@IST.AC.AT

Dingling Yao

*Institute of Science and Technology Austria (ISTA)
3400 Klosterneuburg, Austria*

DINGLING.YAO@IST.AC.AT

Adeel Pervez

*Institute of Science and Technology Austria (ISTA)
3400 Klosterneuburg, Austria*

ADEEL.PERVEZ@IST.AC.AT

Dan Alistarh

*Institute of Science and Technology Austria (ISTA)
3400 Klosterneuburg, Austria*

DAN.ALISTARH@IST.AC.AT

Francesco Locatello

*Institute of Science and Technology Austria (ISTA)
3400 Klosterneuburg, Austria*

FRANCESCO.LOCATELLO@IST.AC.AT

Abstract

We propose *Scalable* Mechanistic Neural Network (S-MNN), an enhanced neural network framework designed for scientific machine learning applications involving long temporal sequences. By reformulating the original Mechanistic Neural Network (MNN) (Pervez et al., 2024), we reduce the computational time and space complexities from cubic and quadratic with respect to the sequence length, respectively, to *linear*. This significant improvement enables efficient modeling of long-term dynamics without sacrificing accuracy or interpretability. Extensive experiments demonstrate that S-MNN matches the original MNN in precision while substantially reducing computational resources. Consequently, S-MNN can drop-in replace the original MNN in applications, providing a practical and efficient tool for integrating mechanistic bottlenecks into neural network models of complex dynamical systems.

1 Introduction

The Mechanistic Neural Network (MNN) (Pervez et al., 2024) has recently emerged as a promising approach in scientific machine learning. Unlike traditional black-box approaches for dynamical systems (Chen et al., 2018, 2021; Kidger et al., 2021; Norcliffe et al., 2020) that primarily focus on forecasting, MNN additionally learns an explicit internal ordinary differential equation (ODE) representation from the noisy observational data that enables various downstream scientific analysis such as parameter identification and causal effect estimation (Yao et al., 2024). Despite their advantages, the original formulation of MNN faces significant scalability challenges. Specifically, the computational time and memory usage severely limit the practical applicability of MNN to problems involving long time horizons or high-resolution temporal data, such as climate recordings (Verma et al., 2024) as the required computations become prohibitive even for the most advanced hardware.

The inefficiency stems from the matrix operations required to solve the linear systems associated with the MNN. In the original framework, two solvers are provided: a *dense* solver and a *sparse* solver. The *dense* solver operates on dense matrices and employs standard methods for solving linear systems, resulting in cubic time and quadratic space complexities with respect to the sequence length. This computational inefficiency makes it unsuitable for long sequences. The MNN *sparse* solver, on the other hand, constructs sparse matrices and uses iterative methods such as the conjugate gradient algorithm to solve the linear systems. While this reduces memory usage by exploiting sparsity, the unstructured sparsity patterns of the matrices prevent the solver from fully leveraging the GPU’s parallelism potential. Additionally, iterative methods can suffer from slow convergence and numerical inaccuracies, particularly for large-scale problems.

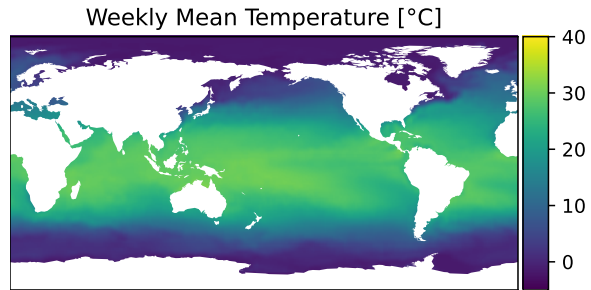


Figure 1: 4-year sea surface temperature (SST) forecasting using the Mechanistic Identifier (Yao et al., 2024) and our *Scalable* Mechanistic Neural Network (S-MNN).

This work proposes a *scalable* variant of MNN (S-MNN) that reduces the computational time and space complexities from cubic and quadratic with respect to the sequence length, respectively, to *linear*, while maintaining on-par accuracy. As a result, we successfully demonstrate the real-world applicability (Figure 1) of S-MNN on long-term climate data that the original MNN failed to handle. Our main contributions are as follows:

- **Complexity Reduction.** We reformulate the original MNN’s underlying linear system by eliminating the slack variables and central difference constraints, and reducing the quadratic programming problem to least squares regression (Section 3.1). This results in the left-hand side square matrix having a banded structure, allowing us to employ efficient algorithms (Section 3.2). The time and space complexities are reduced to *linear* with respect to the sequence length, making it suitable for long-sequence modeling.
- **Efficient Solver Design.** We develop an efficient solver that leverages the inherent sparsity and banded structure of the reformulated linear system (Section 3.2). The solver is optimized for GPU execution, fully exploiting parallelism to achieve significant speed-ups.
- **Long-Term Sequence Modeling for Science.** We validate the effectiveness of our S-MNN through experiments on various benchmarks, including governing equation discovery with the Lorenz system (Section 5.2), solving the Korteweg-de Vries (KdV) partial derivative equation (Section 5.3), and sea surface temperature (SST) prediction for modeling long real-world temporal sequences (Section 5.4). Our results demonstrate that S-MNN matches the precision of the original MNN while significantly reducing computational time and memory usage across the board.

2 Overview of Mechanistic Neural Networks

The Mechanistic Neural Network (MNN) by [Pervez et al. \(2024\)](#) consists of three components: a mechanistic encoder, a specialized differentiable ordinary differential equation (ODE) solver based on constrained optimization, and a mechanistic decoder. The mechanistic encoder, realized as a neural network, generates a semi-symbolic representation of the underlying ODE from an input time series, effectively learning the dynamics from the data. The solver then constructs and solves a linear system that equivalently describes the original system. The mechanistic decoder processes the solver solutions to the final outputs.

For tasks such as forecasting future sequences from past data, the encoder processes the input data to produce the trajectory-specific semi-symbolic representation. Additionally, the encoder can be designed to overcome the limitations of the linear ODE solver by learning parameters of nonlinear basis functions ([Brunton et al., 2016a](#)), enabling the MNN to model nonlinear ODEs effectively. The decoder is optional and their necessity depends on the specific task used for training.

Formally, given a multidimensional discretized time sequence $\mathbf{x}_1, \mathbf{x}_2, \dots, \mathbf{x}_T$ as the input, the mechanistic encoder maps $\mathbf{x}_{1:T}$ into semi-symbolic representations of a set of linear ODEs

$$\sum_{r=0}^R \mathbf{c}_r^\top(t, \mathbf{x}_{1:T}) \frac{d^r \mathbf{y}}{dt^r} = d(t, \mathbf{x}_{1:T}) \quad (1)$$

of the variable $\mathbf{y} \in \mathbb{R}^V$ with the initial conditions

$$\frac{d^r \mathbf{y}}{dt^r} = \mathbf{u}_r(\mathbf{x}_{1:T}) \quad (2)$$

where R is the highest derivative order, $\mathbf{c}_r(t, \mathbf{x}_{1:T}) \in \mathbb{R}^V$ and $d(t, \mathbf{x}_{1:T}) \in \mathbb{R}$ are the coefficients, and $\mathbf{u}_r(\mathbf{x}_{1:T}) \in \mathbb{R}^V$ represents the initial conditions. $\mathbf{c}_r(t, \mathbf{x}_{1:T})$, $d(t, \mathbf{x}_{1:T})$, $\mathbf{u}_r(\mathbf{x}_{1:T})$, as well as the step sizes $s(\mathbf{x}_{1:T})$ for the time discretization are learned by the encoder. The representation θ is compactly denoted as

$$\theta(\mathbf{x}_{1:T}) = \{c(\mathbf{x}_{1:T}), d(\mathbf{x}_{1:T}), u(\mathbf{x}_{1:T}), s(\mathbf{x}_{1:T})\}. \quad (3)$$

The MNN solver then solves the linear ODE using this representation θ , producing the discretized output time sequence $\mathbf{y}_1, \mathbf{y}_2, \dots, \mathbf{y}_T$. The decoder takes $\mathbf{y}_{1:T}$ as input and generates the final output \mathbf{z} . A loss ℓ can be computed based on \mathbf{z} and the target data, and the encoder and decoder networks are updated using gradient descent methods.

An illustrative example is the task of discovering coefficients $\boldsymbol{\xi} \in \mathbb{R}^k$ for a time-independent one-dimensional first-order ODE in the form of

$$dy/dt = g\left(\boldsymbol{\xi}^\top \phi(y)\right) \quad (4)$$

where $\phi: \mathbb{R} \rightarrow \mathbb{R}^k$ is a k dimensional non-linear basis function, $g: \mathbb{R} \rightarrow \mathbb{R}$ is a differentiable function. In this task, we first generate an initial $\boldsymbol{\xi}$ and specify the initial condition $u_{r=0} = x_1$. We fix c to ones where they are multiplied with the first-order derivatives, and zeros otherwise. The step sizes s are determined by the dataset's time increments. During each gradient descent iteration, we set $d = g(\boldsymbol{\xi}^\top \phi(x))$, and then the MNN solver solves for a discretized solution $y_{1:T}$ for Eq. 4. We update $\boldsymbol{\xi}$ by minimizing the loss $\ell = \sum_{t=1}^T \|y_t - x_t\|^2$.

3 Scalable Mechanistic Neural Networks

In this section, we define the linear system for the *Scalable* Mechanistic Neural Network (S-MNN) in Subsection 3.1, and present the solver’s implementation and complexity analysis in Subsection 3.2.

3.1 Linear System Formulation

A linear ordinary differential equation (ODE) system can be characterized by a set of linear equations involving the successive derivatives of an unknown time-dependent function y . Formally, in a system with V variables (output dimensions), derivative orders up to R , and Q governing equations, the state at T discrete time points can be described by a series of clauses

$$\sum_{v=1}^V \sum_{r=0}^R c_{t,q,v,r} y_{t,v,r} = d_{t,q}, \forall t \in \{1, \dots, T\}, q \in \{1, \dots, Q\}, \quad (5)$$

where $y_{t,v,r}$ is the r -th derivative of the v -th variable at t -th time point, $c_{t,q,v,r}$ is the corresponding coefficient for the q -th governing equation, and $d_{t,q}$ is a constant term.

Initial values $u_{t,v,r}$ are specified for each $y_{t,v,r}$ up to time point T_{init} ($1 \leq T_{\text{init}} \leq T$) and derivative order R_{init} ($0 \leq R_{\text{init}} \leq R$):

$$y_{t,v,r} = u_{t,v,r}, \forall t \in \{1, \dots, T_{\text{init}}\}, v \in \{1, \dots, V\}, r \in \{0, \dots, R_{\text{init}}\}. \quad (6)$$

To ensure the smoothness of the trajectory, i.e., that the computed higher-order derivatives are consistent with the derivatives of lower-order terms, we introduce smoothness constraints. We define the forward and backward smoothness constraints using the Taylor expansion of the function y at time points t and $t + 1$ respectively:

$$y_{t+1,v,r} = \sum_{r'=r}^R \frac{s_t^{r'-r}}{(r'-r)!} y_{t,v,r'}, \forall t \in \{1, \dots, T-1\}, v \in \{1, \dots, V\}, r \in \{0, \dots, R\}, \quad (7)$$

$$y_{t,v,r} = \sum_{r'=r}^R \frac{(-s_t)^{r'-r}}{(r'-r)!} y_{t+1,v,r'}, \forall t \in \{1, \dots, T-1\}, v \in \{1, \dots, V\}, r \in \{0, \dots, R\}. \quad (8)$$

where s_t is the time span between time points t and $t + 1$.

Combining the constraints Eqs. 5, 6, 7, and 8 yields a linear system. In total there are m constraints and n unknown variables where

$$m = TQ + T_{\text{init}}V(R_{\text{init}} + 1) + 2(T-1)V(R+1) \text{ and } n = TV(R+1). \quad (9)$$

We arrange the unknown variables $y_{t,v,r}$ into a vector $\mathbf{y} \in \mathbb{R}^n$, the left-hand side coefficients into a matrix $\mathbf{A} \in \mathbb{R}^{m \times n}$, and the right-hand side into a vector $\mathbf{b} \in \mathbb{R}^m$. The linear system can then be compactly represented as $\mathbf{A}\mathbf{y} = \mathbf{b}$.

This system is over-determined ($m > n$) under typical conditions ($T > 1$) and can be solved for \mathbf{y} using least squares regression. To balance the contributions of different constraints, we weight the smoothness constraints (Eqs. 7 and 8) by s_t^r . Additionally, we introduce optional importance weights $w_{\text{gov}}, w_{\text{init}}, w_{\text{smooth}} \in \mathbb{R}$, applied to the governing equations (Eq. 5), initial

conditions (Eq. 6), and smoothness constraints (Eqs. 7 and 8), respectively. This flexibility allows for emphasizing specific aspects of the model during optimization. These weights are encoded into a diagonal matrix \mathbf{W} , and the solution for \mathbf{y} is then given by:

$$\mathbf{y}(c, d, u, s) = \left(\mathbf{A}^\top \mathbf{W} \mathbf{A}\right)^{-1} \mathbf{A}^\top \mathbf{W} \mathbf{b}. \quad (10)$$

Note that \mathbf{y} is differentiable with respect to c , d , u , and s .

Our S-MNN formulation has three key differences from the original MNN formulation in Pervez et al. (2024): (1) the slack variables in the smoothness constraints are removed; (2) the forward and backward smoothness constraints are extended to the highest order ($r = R$), replacing the central difference constraints; (3) the quadratic programming is replaced by a least squares regression.

Also note that, unlike the finite difference method which approximates derivatives by discretizing differential equations, our approach formulates a linear system to directly involve the derivative terms.

3.2 Solver Design, Architecture, and Analysis

The primary motivation for our improvement is our observation that, if we remove the slack variables, the matrix \mathbf{A} will exhibit a specific sparsity pattern that can be exploited for computational and memory gains. A direct implementation based on the dense matrix \mathbf{A} using Eq. 10 incurs cubic time complexity and quadratic space complexity due to matrix multiplication and inversion. However, by analyzing the sparsity pattern of \mathbf{A} , we find that most (e.g., 95% in a typical application) values in the intermediate steps are zero and do not need to be computed or stored. In more detail, Eq. 10 can be decomposed into two steps: (1) a matrix-matrix multiplication $\mathbf{M} = (\mathbf{A}^\top \mathbf{W}) \mathbf{A}$ and a matrix-vector multiplication $\boldsymbol{\beta} = (\mathbf{A}^\top \mathbf{W}) \mathbf{b}$; (2) solving for \mathbf{y} via the linear system $\mathbf{M} \mathbf{y} = \boldsymbol{\beta}$. **The key idea is to structure \mathbf{M} as a banded matrix.** Observing the constraints, we note that the coefficients at time point t are directly related only to those at time points $t-1$, t , and $t+1$. By ordering the variables by t , we can arrange \mathbf{M} into a banded matrix. Specifically, the variable $y_{t,v,r}$ is placed at the position $((t-1)V + v - 1)(R+1) + r + 1$ in the vector \mathbf{y} , and the columns of matrix \mathbf{A} are ordered accordingly. The resulting \mathbf{M} is a symmetric matrix in a block-banded form:

$$\mathbf{M} = \begin{bmatrix} \mathbf{M}_1 & \mathbf{N}_1^\top & & & \\ \mathbf{N}_1 & \mathbf{M}_2 & \ddots & & \\ & \ddots & \ddots & \mathbf{N}_{T-1}^\top & \\ & & & \mathbf{N}_{T-1} & \mathbf{M}_T \end{bmatrix} \quad (11)$$

where each block is a square matrix of size $V(R+1)$. It is important to note that such a banded form is only possible after removing the slack variables from the original MNN formulation, as the slack variables introduce direct relationships between components at all time points.

For the matrix \mathbf{M} , only the non-zero blocks \mathbf{M}_t and \mathbf{N}_t need to be computed and stored. This can be achieved using efficient dense matrix operations with appropriately formatted dependencies c , d , u , and s . The matrix \mathbf{A} does not need to be explicitly constructed. We

present the detailed forward pass calculations for computing \mathbf{M} and $\boldsymbol{\beta}$ in Appendix A.1 and omit them in this subsection. The backward pass is supported by automatic differentiation.

For solving the linear system $\mathbf{M}\mathbf{y} = \boldsymbol{\beta}$, we propose an efficient GPU-friendly algorithm (Algorithm 1). Specifically, we can factorize the positive-definite matrix \mathbf{M} to a banded lower triangular matrix \mathbf{P} and a block diagonal lower triangular matrix \mathbf{L} using blocked versions of LDL and Cholesky decompositions such that

$$\mathbf{P}\mathbf{L}\mathbf{L}^\top\mathbf{P}^\top = \mathbf{M} \quad (12)$$

where \mathbf{P} and \mathbf{L} are partitioned into block matrices in the same form as \mathbf{M} :

$$\mathbf{P} = \begin{bmatrix} \mathbf{I} & & & & \\ \mathbf{P}_1 & \mathbf{I} & & & \\ & \ddots & \ddots & & \\ & & & \mathbf{P}_{T-1} & \mathbf{I} \end{bmatrix} \text{ and } \mathbf{L} = \begin{bmatrix} \mathbf{L}_1 & & & & \\ & \mathbf{L}_2 & & & \\ & & \ddots & & \\ & & & \ddots & \\ & & & & \mathbf{L}_T \end{bmatrix}. \quad (13)$$

with each block as a square matrix of size $V(R+1)$ and the diagonal blocks of \mathbf{P} as an identity matrix \mathbf{I} . We also partition $\boldsymbol{\beta}$ and \mathbf{y} into sub-vectors, $\boldsymbol{\beta} = [\boldsymbol{\beta}_1^\top, \boldsymbol{\beta}_2^\top, \dots, \boldsymbol{\beta}_T^\top]^\top$ and $\mathbf{y} = [\mathbf{y}_1^\top, \mathbf{y}_2^\top, \dots, \mathbf{y}_T^\top]^\top$. We then use forward and backward substitution to solve the following sequence of equations:

$$\mathbf{P}\boldsymbol{\beta}' = \boldsymbol{\beta}, \quad \mathbf{L}\boldsymbol{\beta}'' = \boldsymbol{\beta}', \quad \mathbf{L}^\top\boldsymbol{\beta}''' = \boldsymbol{\beta}'', \quad \mathbf{P}^\top\mathbf{y} = \boldsymbol{\beta}'''. \quad (14)$$

The main advantage of this algorithm is that only the blocks \mathbf{P}_t and \mathbf{L}_t in the matrices \mathbf{P} and \mathbf{L} need to be computed and stored, which limits the computational complexities of the LDL and Cholesky decompositions and the subsequent forward and backward substitutions to be linear in T . In contrast, explicitly computing \mathbf{M}^{-1} or \mathbf{L}^{-1} would involve dense or triangular-dense full-size matrices and should be avoided.

Interestingly, for the backward pass of $\mathbf{M}\mathbf{y} = \boldsymbol{\beta}$, the back-propagated gradients of \mathbf{M} and $\boldsymbol{\beta}$ have elegant analytic solutions that enable further (constant factor) speed-ups compared to automatic differentiation. Assuming that the final loss is ℓ , and given $\partial\ell/\partial\mathbf{y}$, the gradients are

$$\frac{\partial\ell}{\partial\boldsymbol{\beta}} = \mathbf{M}^{-1}\frac{\partial\ell}{\partial\mathbf{y}} \quad \text{and} \quad \frac{\partial\ell}{\partial\mathbf{M}} = -\frac{\partial\ell}{\partial\boldsymbol{\beta}}\mathbf{y}^\top. \quad (15)$$

The proof can be found in Appendix A.2. Algorithm 2 details the backward pass. Computing $\partial\ell/\partial\boldsymbol{\beta}$ involves solving a similar linear system using the banded matrix \mathbf{M} , and $\partial\ell/\partial\mathbf{M}$ is a vector outer product that can be efficiently computed for the non-zero blocks \mathbf{M}_t and \mathbf{N}_t . The matrices \mathbf{P} , \mathbf{L} , and the solution \mathbf{y} can be stored during the forward pass and reused for the backward pass.

Numerical Stability Considerations. An important aspect of our solver design is the numerical stability offered by the direct method of Cholesky decomposition compared to iterative methods like the conjugate gradient (CG) algorithm. Both direct and iterative methods have errors influenced by the condition number κ of the matrix. However, direct methods tend to be more stable in practice because they compute an exact solution up to

<hr/> <p>Algorithm 1: Solver Forward Pass</p> <p>Input: $M_{1:T}, N_{1:T-1}, \beta_{1:T}$</p> <p>Output: $L_{1:T}, P_{1:T-1}, y_{1:T}$</p> <p>1 $L_{1:T}, P_{1:T-1}$ \leftarrow DECOMPOSE ($M_{1:T}, N_{1:T-1}$);</p> <p>2 $y_{1:T} \leftarrow$ SUBSTITUTE ($L_{1:T}, P_{1:T-1}, \beta_{1:T}$);</p> <hr/>	<hr/> <p>Algorithm 2: Solver Backward Pass</p> <p>Input: $L_{1:T}, P_{1:T-1}, y_{1:T}, \frac{\partial \ell}{\partial y_{1:T}}$</p> <p>Output: $\frac{\partial \ell}{\partial M_{1:T}}, \frac{\partial \ell}{\partial N_{1:T-1}}, \frac{\partial \ell}{\partial \beta_{1:T}}$</p> <p>1 $\frac{\partial \ell}{\partial \beta_{1:T}}$ \leftarrow SUBSTITUTE ($L_{1:T}, P_{1:T-1}, \frac{\partial \ell}{\partial y_{1:T}}$);</p> <p>2 for $i \leftarrow 1$ to T <i>in parallel</i> do</p> <p>3 $\frac{\partial \ell}{\partial M_i} \leftarrow -\frac{\partial \ell}{\partial \beta_i} y_i^\top$;</p> <p>4 end</p> <p>5 for $i \leftarrow 1$ to $T-1$ <i>in parallel</i> do</p> <p>6 $\frac{\partial \ell}{\partial N_i} \leftarrow -\frac{\partial \ell}{\partial \beta_{i+1}} y_i^\top - y_{i+1} \frac{\partial \ell}{\partial \beta_i^\top}$;</p> <p>7 end</p> <hr/>
<hr/> <p>Algorithm 3: Decompose</p> <p>Input: $M_{1:T}, N_{1:T-1}$</p> <p>Output: $L_{1:T}, P_{1:T-1}$</p> <p>1 $L_{1:T}, P_{1:T-1} \leftarrow M_{1:T}, N_{1:T-1}$;</p> <p>2 for $i \leftarrow 1$ to T do</p> <p style="padding-left: 20px;">/* blockwise Cholesky */</p> <p>3 if $i > 1$ then</p> <p style="padding-left: 40px;">4 $P_{i-1} \leftarrow P_{i-1} L_{i-1}^{-\top}$;</p> <p style="padding-left: 40px;">5 $L_i \leftarrow L_i - P_{i-1} P_{i-1}^\top$;</p> <p>6 end</p> <p>7 $L_i \leftarrow$ CHOLESKY (L_i); // standard Cholesky</p> <p>8 end</p> <p>9 for $i \leftarrow 1$ to $T-1$ <i>in parallel</i> do</p> <p style="padding-left: 20px;">/* to blockwise LDL */</p> <p>10 $P_i \leftarrow P_i L_i^{-1}$;</p> <p>11 end</p> <hr/>	<hr/> <p>Algorithm 4: Substitute</p> <p>Input: $L_{1:T}, P_{1:T-1}, \alpha_{1:T}$</p> <p>Output: $\alpha_{1:T}$</p> <p>1 for $i \leftarrow 2$ to T do</p> <p style="padding-left: 20px;">/* forward substitute */</p> <p>2 $\alpha_i \leftarrow \alpha_i - P_{i-1} \alpha_{i-1}$;</p> <p>3 end</p> <p>4 for $i \leftarrow 1$ to T <i>in parallel</i> do</p> <p>5 $\alpha_i \leftarrow L_i^{-\top} (L_i^{-1} \alpha_i)$;</p> <p>6 end</p> <p>7 for $i \leftarrow T-1$ to 1 do</p> <p style="padding-left: 20px;">/* backward substitute */</p> <p>8 $\alpha_i \leftarrow \alpha_i - P_i^\top \alpha_{i+1}$;</p> <p>9 end</p> <hr/>

machine precision. In contrast, CG is iterative and can suffer from error accumulation across iterations, especially when the matrix is ill-conditioned or when the number of iterations is limited for computational reasons. This is crucial in our applications, where accurate solutions are necessary for modeling chaotic systems.

Complexity Analysis. The original MNN *dense* (exact) solver described in Pervez et al. (2024) has time complexity $O(T^3 V^3 R^3)$ and space complexity $O(T^2 V^2 R^2)$, for time T , V variables, and R derivative orders. The original *sparse* (approximate) solver working via conjugate gradient has both time and space complexities $O(T^2 V^2 R^2)$. In our proposed exact S-MNN, the time complexity is reduced by a $\Theta(T^2)$ factor to $O(TV^3 R^3)$ from the MNN *dense* solver, and the space complexity is reduced to $O(TV^2 R^2)$. Thus, both time and memory requirements now depend *linearly* on the number of time points T , making the new method more scalable for longer trajectories.

4 Related Work in Scientific Machine Learning

Scientific machine learning has emerged as a transformative field that combines data-driven approaches with domain-specific knowledge to model complex dynamical systems. Various specialized methodologies have been developed to tackle different aspects of this challenge, particularly in solving differential equations using neural networks and, to a lesser extent, inverse problems.

Models for Prediction. Neural Ordinary Differential Equations (Neural ODEs) (Chen et al., 2018, 2021; Kidger et al., 2021; Norcliffe et al., 2020) model continuous-time dynamics by parameterizing the derivative of the hidden state with a neural network. Neural ODEs, however, are constrained by the structure and sequential nature of ODE solvers and can be inefficient to train. Neural Operators (Li et al., 2020b,a, 2024, 2021; Azizzadenesheli et al., 2024; Boullé & Townsend, 2023) are designed to learn mappings between infinite-dimensional function spaces, enabling the modeling of PDEs and complex spatial-temporal patterns. However, their focus on lower frequencies in the Fourier spectrum can lead to poor prediction over longer roll-outs (Lippe et al., 2023).

Models for Discovery. The line of work on Sparse Identification of Nonlinear Dynamical Systems (SINDy) (Kaheman et al., 2020; Brunton et al., 2016b,a; Kaptanoglu et al., 2021; Course & Nair, 2023; Lu et al., 2022; Rudy et al., 2017) aims to discover governing equations by identifying sparse representations within a *predefined* library of candidate functions. However, SINDy is only a generalized linear model that does not use neural networks and can struggle with highly complex, noisy, or strongly nonlinear systems. Physics-informed networks and universal differential equations (Raissi et al., 2019; Rackauckas et al., 2020) also work as discovery methods for inferring unknown terms in PDEs. Symbolic regression methods (Udrescu & Tegmark, 2020; d’Ascoli et al., 2023) constitute another line of work that aims to discover purely symbolic expressions from data.

Discussion. Mechanistic Neural Networks (MNNs) (Pervez et al., 2024) have been proposed as a single framework for prediction and discovery. MNNs compute ODE representations from data which provide a strong inductive bias for scientific ML tasks. However, MNN training introduces significant challenges that require solving large linear systems during both the forward and backward passes and demands substantial computational resources. Our method addresses this scalability problem by reducing the computational complexity and enables applications on long sequences.

5 Experiments

To demonstrate the effectiveness and scalability of our proposed *Scalable* Mechanistic Neural Network (S-MNN), we conduct experiments across multiple settings in scientific machine learning applications for dynamical systems including governing equation discovery for the Lorenz system (Section 5.2), solving the Korteweg-de Vries (KdV) partial derivative equation (PDE) (Section 5.3), and sea surface temperature (SST) prediction for modeling long real-world temporal sequences (Section 5.4). We show that S-MNN matches the precisions and convergence rates of the original MNN (Pervez et al., 2024) while significantly reducing computational time and GPU memory usage.

5.1 Standalone Validation

To assess the correctness of our solver in solving linear ordinary differential equations (ODEs), we conducted a standalone validation. Our solver is designed to solve linear ODEs directly (Section 3.1) without incorporating additional neural network layers or trainable parameters.

Experiment Settings. We selected five linear ODE problems from ODEBench (d’Ascoli et al., 2024)—RC Circuit, Population Growth, Language Death Model, Harmonic Oscillator, and Harmonic Oscillator with Damping—that are commonly used in various scientific fields such as physics and biology, along with an additional third-order ODE. Mathematical details about these ODEs are provided in the Appendix B.1. For each problem, we discretized the time axis into 1,000 steps with a uniform step size of 0.01 and applied our S-MNN solver.

Results and Discussion. We compared the numerical solutions obtained by our solver against the corresponding closed-form solutions. Figure 2 presents the results, where we plot the solutions $y(t)$ along with their first and second derivatives $y'(t)$ and $y''(t)$. The numerical results from our solver closely match the analytical solutions, exhibiting negligible differences (mean squared error $< 10^{-6}$ in all cases, $< 10^{-8}$ in most cases). These results confirm that our solver is capable of correctly solving linear ODEs.

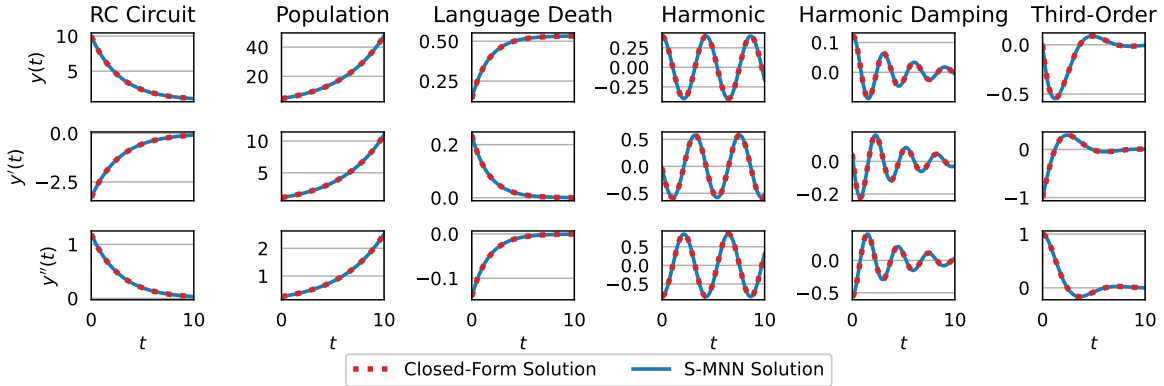


Figure 2: Standalone S-MNN solver validation results compared with the closed-form solutions.

5.2 Comparative Analysis: Discovery of Governing Equations

In this experiment, we evaluate the capability of our S-MNN in discovering the coefficients of the governing equations for the Lorenz system following Section 5.1 in the origin MNN paper (Pervez et al., 2024). The Lorenz system is a set of nonlinear ODEs known for its chaotic behavior, making it a standard benchmark for testing equation discovery methods in dynamical systems. The governing equations are given by

$$\begin{cases} dx/dt = \sigma(y - x) = a_1x + a_2y \\ dy/dt = x(\rho - z) - y = a_3x + a_4y + a_5xz \\ dz/dt = xy - \beta z = a_6z + a_7xy \end{cases} \quad (16)$$

where $a_1, \dots, a_7 \in \mathbb{R}$ are the coefficients to be discovered.

Dataset. The dataset was generated by numerically integrating the Lorenz system equations using the standard parameters $\sigma = 10$, $\rho = 28$, and $\beta = 8/3$. We used the initial condition $x = y = z = 1$ and integrated over 10,000 time steps with a step size of 0.01 using the `scipy.integrate.odeint` function.

Experiment Settings. We applied our solver to the same network architecture and dataset in Pervez et al. (2024). We trained the model with the default settings: sequence length of 50 and batch size of 512. The training objective was to minimize the difference between the predicted and true trajectories by optimizing the coefficients a_1, \dots, a_7 . Then, to assess the scalability of our method, we measured runtime and GPU memory consumption across different sequence lengths and batch sizes using an NVIDIA H100 GPU with 80 GB of memory.

Results and Discussion. Figure 3 shows the convergence of the loss over the optimization steps using our S-MNN solver compared to the original MNN *dense* and *sparse* solvers. The results indicate that our S-MNN solver achieves similar convergence rates, confirming that the removal of slack variables does not adversely affect accuracy. The final results of the discovered coefficients a_0, \dots, a_7 are recorded in Appendix B.2.

Table 1 summarizes the performance and GPU memory usage. Our S-MNN solver not only maintains high accuracy but also offers substantial efficiency improvements. Specifically, compared to the MNN *dense* solver, our method achieves a 4.9× speedup and reduces GPU memory usage by 50% for the default setting (batch size 512, sequence length 50). The more significant improvement in runtime compared to memory usage is expected, as our approach reduces runtime from $O(T^3)$ to $O(T)$, and memory from $O(T^2)$ to $O(T)$, with T denoting the sequence length. Our S-MNN solver maintains high performance even with larger batch sizes and sequence lengths where the MNN solvers run out of memory or become computationally infeasible.

5.3 Comparative Analysis: Solving Partial Differential Equations (PDEs)

Next, we evaluate the capability of our S-MNN in solving partial differential equations (PDE), specifically focusing on the Korteweg-De Vries (KdV) equation, which is a third-order nonlinear PDE that describes the propagation of waves in shallow water and is expressed as

$$\frac{\partial y}{\partial t} + \frac{\partial^3 y}{\partial x^3} - 6y \frac{\partial y}{\partial x} = 0, \tag{17}$$

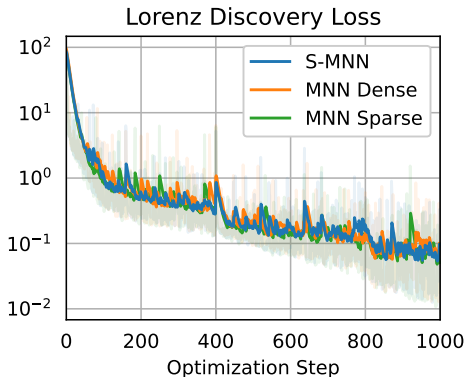


Figure 3: Lorenz discovery loss over first 1,000 optimization steps (exponential moving average factor = 0.9) using S-MNN (ours) compared with the original MNN *dense* and *sparse* solvers (Pervez et al., 2024).

Table 1: Performance and GPU memory usage comparison for the Lorenz discovery experiment.

Batch Size		512	512	512	64	4096
Sequence Length		50	5	500	50	50
Time per Optimization Step [ms]	MNN Dense	36.4	9.5	N/A ¹	10.0	208.1
	MNN Sparse	104.4	76.5	>589.7 ²	80.5	406.8
	<i>S-MNN</i>	7.4	5.5	32.2	5.5	18.3
GPU Memory Usage [GiB]	MNN Dense	2.77	1.18	>80.00 ¹	1.33	14.85
	MNN Sparse	1.69	0.93	9.83 ²	0.96	7.96
	<i>S-MNN</i>	1.38	1.32	1.96	1.33	1.81

¹Out of memory error. ²Loss does not converge after a large number (200) of conjugate gradient iterations.

where $y(x, t)$ represents the wave amplitude as a function of spatial coordinate x and time t . Solving the KdV equation is challenging due to its nonlinearity and the involvement of higher-order spatial derivatives, making it a popular benchmark for PDEs.

Dataset. We consider the KdV dataset provided by Brandstetter et al. (2022). The dataset consists of 512 samples each for training, validation, and testing. Each sample has a spatial domain of 256 meters and a temporal domain of 140 seconds, discretized into 256 spatial points and 140 temporal steps.

Experiment Settings. We model the temporal evolution at each spatial point as an independent ODE. A ResNet-1D architecture (Brandstetter et al., 2022) is employed to encode the temporal and spatial dependencies in the input sequences and feed them into the mechanistic solver. The sequence length is set to 10 seconds, and the model is trained to predict the wave profile over the next 9 seconds. The model is trained for 800 epochs. We repeat the same experiment for the original MNN *dense* and *sparse* solvers as well as our S-MNN solver.

Results and Discussion. Figure 4 illustrates a comparison between the ground truth solution, the prediction obtained from the original MNN *dense* solver, and that from our S-MNN. Both models produce predictions that closely align with the ground truth, demonstrating that our S-MNN effectively captures the intricate dynamics of the KdV equation. The MNN *sparse* solver cannot converge in this experiment and its result is not shown.

Table 2 presents a summary of the testing error, end-to-end training time, and GPU memory usage for each method. Our S-MNN achieves an RMSE (relative mean squared error) of 0.0042, slightly improving upon the 0.0046 of the MNN *dense* solver. In terms of efficiency, the training time for S-MNN is significantly reduced to 10.1 hours compared to 38.0 hours for the MNN *dense* solver, indicating a substantial speedup. Additionally, our method consumes less GPU memory, using 2.19 GiB versus 3.40 GiB for the original solver. The MNN *sparse* solver did not converge within a reasonable time frame, taking 82.4 hours without achieving satisfactory results.

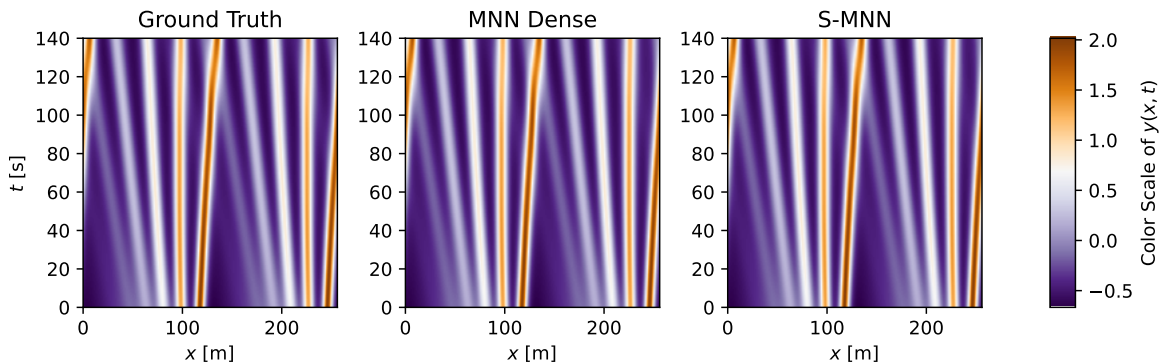


Figure 4: Visual comparison between the ground truth, the MNN *dense* solver (Pervez et al., 2024) prediction, and our S-MNN prediction for the KdV equation.

Table 2: Testing error, end-to-end training time, and GPU training memory usage for KdV.

Method	RMSE	Training Time [hour]	GPU Memory [GiB]
MNN Dense	0.0046	38.0	3.40
MNN Sparse	Did Not Converge	82.4	3.07
<i>S-MNN</i>	0.0042	10.1	2.19

5.4 Real-world Application: Long-term Sea Surface Temperature Forecasting

The ability to handle longer sequences and larger batch sizes without sacrificing performance positions our S-MNN as a powerful tool for modeling complex dynamical systems. In this section, we demonstrate a real-world example use case: sea surface temperature (SST) prediction. SST exhibits long periodic features that can only be effectively captured with long sequences.

Dataset. We use the SST-V2 dataset (Huang et al., 2021), which provides weekly mean sea surface temperatures for 1,727 weeks from December 31, 1989, to January 29, 2023, over a 1° latitude \times 1° longitude global grid (180×360).

Experiment Settings. We employ the Mechanistic Identifier proposed by Yao et al. (2024) to predict SST data. The model leverages mechanistic layers to capture the underlying

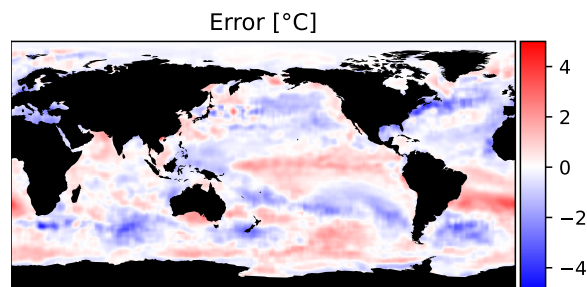


Figure 5: Error visualization for the S-MNN 4-year sea surface temperature (SST) prediction.

dynamics of SST. We set the default batch size to 12,960 (corresponding to 6,480 pairs of grid points and their randomly selected neighboring points) and the sequence length (chunk length) to 208 weeks. The dataset is split so that the latest chunk of measurements is reserved for testing while the remaining data is used for training. The model is trained for 1,000 epochs. To evaluate the scalability and stability, we benchmark the model with different sequence lengths.

Results and Discussion. Figure 1 visualizes the 4-year (208 weeks) prediction made by our S-MNN using the Mechanistic Identifier. Figure 5 visualizes its prediction error over the ground truth. The S-MNN effectively captures the spatial patterns of SST, demonstrating high predictive precision.

To quantitatively assess the performance and scalability of our S-MNN, we measure the accuracy in terms of the mean squared error (MSE) over the standardized data, as well as the runtime and GPU memory usage across different sequence lengths. For comparison, we also perform the experiment using the MNN *dense* solver for smaller sequences. Figure 6 summarizes these results.

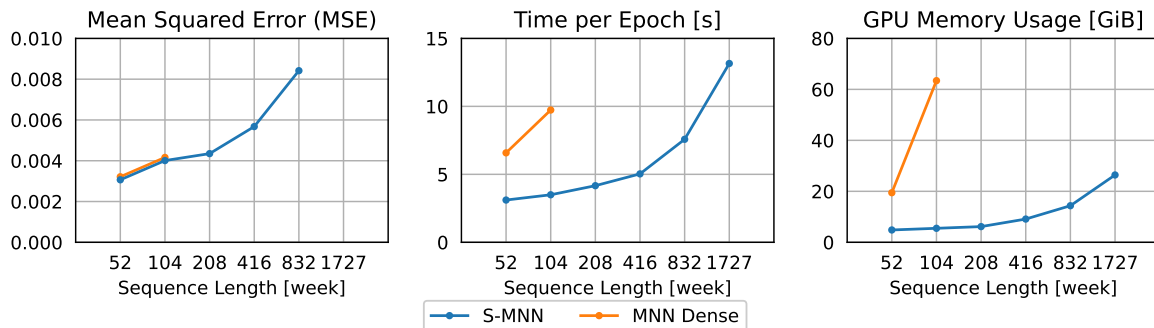


Figure 6: Testing error, training runtime, and GPU training memory usage comparisons between S-MNN (ours) and MNN *dense* solver (Pervez et al., 2024) for SST forecasting. Note that the x-axis is in log scale, so both runtime and memory consumption increase linearly as expected.

We observe that the MSE (averaged over both sequence length and batch size) remains low for both the MNN *dense* and S-MNN solvers, with our S-MNN maintaining low MSE even for longer sequences where the MNN *dense* solver cannot run due to resource limitations. A slight increase in MSE for longer sequences is expected, as modeling longer-term dependencies introduces increased complexity, and the error accumulates over extended prediction horizons. Note that for the sequence length of 1,727, we used the entire dataset for training, leaving no separate testing dataset for evaluation, which is why no MSE results can be provided in Figure 6. Given the log-scale in the x-axis, we observe that S-MNN demonstrates a linear increase in both runtime and memory consumption with respect to sequence length, aligning with our theoretical complexities for time and space. In contrast, the MNN *dense* solver exhibits a much steeper increase in memory usage due to its quadratic space complexity, quickly exceeding the 80 GiB limit of our GPU for longer sequences. We were unable to run it for sequence lengths beyond 104 weeks. We also tested the MNN *sparse* solver, which was too slow to complete the experiment in any reasonable time.

6 Conclusion

This paper introduced the *Scalable* Mechanistic Neural Network (S-MNN), addressing the scalability limitations of the original Mechanistic Neural Networks (Pervez et al., 2024) (MNN) by reducing computational complexities to *linear* in sequence length for both time and space. This was achieved by eliminating slack variables and central difference constraints, transitioning from quadratic programming to least squares regression, and exploiting banded matrix structures within the solver. Our experiments demonstrated that S-MNN retains the precision of the original MNN while significantly enhancing computational efficiency. Given these substantial advantages, S-MNN can drop-in replace the original MNN. We believe this advancement can provide a practical and efficient method for embedding mechanistic knowledge into neural network models for complex dynamical systems.

Limitations and Future Work. While our S-MNN significantly enhances scalability, certain components, such as the sequential for-loops in the Cholesky decomposition (Algorithm 3) and the forward/backward substitution steps (Algorithm 4), still limit parallelism along the time dimension due to inherent data dependencies. This sequential execution can become a bottleneck when the batch and block sizes are small compared to the number of time steps, leading to underutilization of GPU resources and increased CPU overhead from launching small GPU kernels. Although we have employed CUDA Graphs to reduce this overhead, the fundamental sequential nature of the algorithms remains unaddressed. For future work, we aim to develop algorithms that retain linear time and space complexities but introduce full parallelism also across the time dimension.

References

- Kamyar Azizzadenesheli, Nikola Kovachki, Zongyi Li, Miguel Liu-Schiaffini, Jean Kossaifi, and Anima Anandkumar. Neural operators for accelerating scientific simulations and design. *Nature Reviews Physics*, pp. 1–9, 2024. 8
- Nicolas Boullé and Alex Townsend. A mathematical guide to operator learning. *arXiv preprint arXiv:2312.14688*, 2023. 8
- Johannes Brandstetter, Max Welling, and Daniel E. Worrall. Lie point symmetry data augmentation for neural PDE solvers. In Kamalika Chaudhuri, Stefanie Jegelka, Le Song, Csaba Szepesvári, Gang Niu, and Sivan Sabato (eds.), *International Conference on Machine Learning, ICML 2022, 17-23 July 2022, Baltimore, Maryland, USA*, volume 162 of *Proceedings of Machine Learning Research*, pp. 2241–2256. PMLR, 2022. URL <https://proceedings.mlr.press/v162/brandstetter22a.html>. 11
- Steven L Brunton, Joshua L Proctor, and J Nathan Kutz. Discovering governing equations from data by sparse identification of nonlinear dynamical systems. *Proceedings of the national academy of sciences*, 113(15):3932–3937, 2016a. 3, 8, 20
- Steven L Brunton, Joshua L Proctor, and J Nathan Kutz. Sparse identification of nonlinear dynamics with control (sindyc). *IFAC-PapersOnLine*, 49(18):710–715, 2016b. 8
- Ricky T. Q. Chen, Yulia Rubanova, Jesse Bettencourt, and David Duvenaud. Neural ordinary differential equations. *Advances in Neural Information Processing Systems*, 2018. 1, 8

- Ricky T. Q. Chen, Brandon Amos, and Maximilian Nickel. Learning neural event functions for ordinary differential equations. *International Conference on Learning Representations*, 2021. 1, 8
- Kevin Course and Prasanth B Nair. State estimation of a physical system with unknown governing equations. *Nature*, 622(7982):261–267, 2023. 8
- Stéphane d’Ascoli, Sören Becker, Alexander Mathis, Philippe Schwaller, and Niki Kilbertus. Odeformer: Symbolic regression of dynamical systems with transformers. *arXiv preprint arXiv:2310.05573*, 2023. 8
- Stéphane d’Ascoli, Sören Becker, Philippe Schwaller, Alexander Mathis, and Niki Kilbertus. Odeformer: Symbolic regression of dynamical systems with transformers. In *The Twelfth International Conference on Learning Representations, ICLR 2024, Vienna, Austria, May 7-11, 2024*. OpenReview.net, 2024. URL <https://openreview.net/forum?id=TzoHLiGVMo>. 9, 19
- Boyin Huang, Chunying Liu, Viva Banzon, Eric Freeman, Garrett Graham, Bill Hankins, Tom Smith, and Huai-Min Zhang. Improvements of the daily optimum interpolation sea surface temperature (doisst) version 2.1. *Journal of Climate*, 34(8):2923 – 2939, 2021. doi: 10.1175/JCLI-D-20-0166.1. URL <https://journals.ametsoc.org/view/journals/clim/34/8/JCLI-D-20-0166.1.xml>. 12
- Kadierdan Kaheman, J Nathan Kutz, and Steven L Brunton. Sindy-pi: a robust algorithm for parallel implicit sparse identification of nonlinear dynamics. *Proceedings of the Royal Society A*, 476(2242):20200279, 2020. 8
- Alan A Kaptanoglu, Jared L Callahan, Aleksandr Aravkin, Christopher J Hansen, and Steven L Brunton. Promoting global stability in data-driven models of quadratic nonlinear dynamics. *Physical Review Fluids*, 6(9):094401, 2021. 8
- Patrick Kidger, Ricky T. Q. Chen, and Terry J. Lyons. "hey, that’s not an ode": Faster ode adjoints via seminorms. *International Conference on Machine Learning*, 2021. 1, 8
- Zongyi Li, Nikola Kovachki, Kamyar Azizzadenesheli, Burigede Liu, Kaushik Bhattacharya, Andrew Stuart, and Anima Anandkumar. Neural operator: Graph kernel network for partial differential equations. *arXiv preprint arXiv:2003.03485*, 2020a. 8
- Zongyi Li, Nikola Kovachki, Kamyar Azizzadenesheli, Burigede Liu, Andrew Stuart, Kaushik Bhattacharya, and Anima Anandkumar. Multipole graph neural operator for parametric partial differential equations. *Advances in Neural Information Processing Systems*, 33: 6755–6766, 2020b. 8
- Zongyi Li, Nikola Borislavov Kovachki, Kamyar Azizzadenesheli, Burigede Liu, Kaushik Bhattacharya, Andrew M. Stuart, and Anima Anandkumar. Fourier neural operator for parametric partial differential equations. In *9th International Conference on Learning Representations, ICLR 2021, Virtual Event, Austria, May 3-7, 2021*. OpenReview.net, 2021. URL <https://openreview.net/forum?id=c8P9NQVtmn0>. 8

- Zongyi Li, Hongkai Zheng, Nikola Kovachki, David Jin, Haoxuan Chen, Burigede Liu, Kamyar Azizzadenesheli, and Anima Anandkumar. Physics-informed neural operator for learning partial differential equations. *ACM/JMS Journal of Data Science*, 1(3):1–27, 2024. 8
- Phillip Lippe, Bastiaan S. Veeling, Paris Perdikaris, Richard E Turner, and Johannes Brandstetter. PDE-Refiner: Achieving Accurate Long Rollouts with Neural PDE Solvers. In *Thirty-seventh Conference on Neural Information Processing Systems*, 2023. URL <https://openreview.net/forum?id=Qv646811WS>. 8
- Peter Y Lu, Joan Ariño Bernad, and Marin Soljačić. Discovering sparse interpretable dynamics from partial observations. *Communications Physics*, 5(1):206, 2022. 8
- Alexander Norcliffe, Cristian Bodnar, Ben Day, Nikola Simidjievski, and Pietro Liò. On second order behaviour in augmented neural odes. *Advances in neural information processing systems*, 33:5911–5921, 2020. 1, 8
- Adeel Pervez, Francesco Locatello, and Stratis Gavves. Mechanistic neural networks for scientific machine learning. In *Forty-first International Conference on Machine Learning, ICML 2024, Vienna, Austria, July 21-27, 2024*. OpenReview.net, 2024. URL <https://openreview.net/forum?id=pLtuwhoQh7>. 1, 3, 5, 7, 8, 9, 10, 12, 13, 14
- Christopher Rackauckas, Yingbo Ma, Julius Martensen, Collin Warner, Kirill Zubov, Rohit Supekar, Dominic Skinner, and Ali Jasim Ramadhan. Universal differential equations for scientific machine learning. *CoRR*, abs/2001.04385, 2020. URL <https://arxiv.org/abs/2001.04385>. 8
- M. Raissi, P. Perdikaris, and G.E. Karniadakis. Physics-informed neural networks: A deep learning framework for solving forward and inverse problems involving nonlinear partial differential equations. *Journal of Computational Physics*, 378:686–707, 2019. ISSN 0021-9991. doi: <https://doi.org/10.1016/j.jcp.2018.10.045>. URL <https://www.sciencedirect.com/science/article/pii/S0021999118307125>. 8
- Samuel H Rudy, Steven L Brunton, Joshua L Proctor, and J Nathan Kutz. Data-driven discovery of partial differential equations. *Science advances*, 3(4):e1602614, 2017. 8
- Silviu-Marian Udrescu and Max Tegmark. Ai feynman: A physics-inspired method for symbolic regression. *Science Advances*, 6(16):eaay2631, 2020. 8
- Yogesh Verma, Markus Heinonen, and Vikas Garg. Climode: Climate and weather forecasting with physics-informed neural odes. *arXiv preprint arXiv:2404.10024*, 2024. 1
- Dingling Yao, Caroline Muller, and Francesco Locatello. Marrying causal representation learning with dynamical systems for science. *Advances in Neural Information Processing Systems*, 37, 2024. 1, 2, 12

Appendix A. Theoretical Derivations

A.1 Compute M and β

Define matrix $\mathbf{C}_t \in \mathbb{R}^{Q \times V(R+1)}$ such that $[\mathbf{C}_t]_{q,i} = c_{t,q,v,r}$ where $v = \lfloor (i-1)/(R+1) \rfloor + 1$ and $r = (i-1) \bmod (R+1)$.

Define vector $\mathbf{d}_t = [d_{t,1}, d_{t,2}, \dots, d_{t,Q}]^\top \in \mathbb{R}^Q$.

Define constant matrix $\mathbf{U}_t \in \{0, 1\}^{V(R+1) \times V(R+1)}$ such that

$$[\mathbf{U}_t]_{i,j} = \begin{cases} 1 & \text{if } t \leq T_{\text{init}} \text{ and } ((i-1) \bmod (R+1)) \leq R_{\text{init}} \text{ and } i = j, \\ 0 & \text{otherwise.} \end{cases} \quad (18)$$

Define vector $\mathbf{u}_t \in \mathbb{R}^{V(R+1)}$ such that

$$[\mathbf{u}_t]_i = \begin{cases} u_{t,v,r} & \text{if } t \leq T_{\text{init}} \text{ and } r \leq R_{\text{init}}, \\ 0 & \text{otherwise,} \end{cases} \quad (19)$$

where $v = \lfloor (i-1)/(R+1) \rfloor + 1$ and $r = (i-1) \bmod (R+1)$.

Define constant matrix $\mathbf{F} \in \mathbb{R}^{(R+1) \times (R+1)}$ such that

$$[\mathbf{F}]_{i,j} = \begin{cases} 0 & \text{if } i > j, \\ 1/(j-i)! & \text{otherwise.} \end{cases} \quad (20)$$

Define matrix $\mathbf{S}_t^+ = \text{diag}(s_t^0, s_t^1, \dots, s_t^R) \in \mathbb{R}^{(R+1) \times (R+1)}$.

Define matrix $\mathbf{S}_t^- = \text{diag}((-s_t)^0, (-s_t)^1, \dots, (-s_t)^R) \in \mathbb{R}^{(R+1) \times (R+1)}$.

Define matrix $\mathbf{S}_t^2 = \text{diag}(s_t^0, s_t^2, \dots, s_t^{2R}) \in \mathbb{R}^{(R+1) \times (R+1)}$.

Define matrix $\mathbf{S}_t^* \in \mathbb{R}^{(R+1) \times (R+1)}$ such that

$$\mathbf{S}_t^* = \begin{cases} (\mathbf{S}_1^+)^{\top} \mathbf{F}^{\top} \mathbf{F} \mathbf{S}_1^+ + \mathbf{S}_1^2 & \text{if } t = 1, \\ (\mathbf{S}_{T-1}^-)^{\top} \mathbf{F}^{\top} \mathbf{F} \mathbf{S}_{T-1}^- + \mathbf{S}_{T-1}^2 & \text{if } t = T, \\ (\mathbf{S}_t^+)^{\top} \mathbf{F}^{\top} \mathbf{F} \mathbf{S}_t^+ + (\mathbf{S}_{t-1}^-)^{\top} \mathbf{F}^{\top} \mathbf{F} \mathbf{S}_{t-1}^- + \mathbf{S}_t^2 + \mathbf{S}_{t-1}^2 & \text{otherwise.} \end{cases} \quad (21)$$

Define matrix $\mathbf{S}_t^{**} = -(\mathbf{S}_t^+)^{\top} \mathbf{F} \mathbf{S}_t^+ - (\mathbf{S}_t^-)^{\top} \mathbf{F}^{\top} \mathbf{S}_t^- \in \mathbb{R}^{(R+1) \times (R+1)}$.

Define block diagonal matrix $\mathbf{S}_t = \text{Diag}(\underbrace{\mathbf{S}_t^*, \dots, \mathbf{S}_t^*}_{V \text{ times}}) \in \mathbb{R}^{V(R+1) \times V(R+1)}$.

Then, $\mathbf{M}_{t,t}$, $\mathbf{M}_{t+1,t}$, and β_t can be computed as

$$\mathbf{M}_{t,t} = w_{\text{gov}}^2 \mathbf{C}_t^{\top} \mathbf{C}_t + w_{\text{init}}^2 \mathbf{U}_t + w_{\text{smooth}}^2 \mathbf{S}_t, \forall t \in \{1, \dots, T\}, \quad (22)$$

$$\mathbf{M}_{t+1,t} = w_{\text{smooth}}^2 \text{Diag}(\underbrace{\mathbf{S}_t^{**}, \dots, \mathbf{S}_t^{**}}_{V \text{ times}}), \forall t \in \{1, \dots, T-1\}, \quad (23)$$

$$\beta_t = w_{\text{gov}}^2 \mathbf{C}_t^{\top} \mathbf{d}_t + w_{\text{init}}^2 \mathbf{u}_t, \forall t \in \{1, \dots, T\}. \quad (24)$$

A.2 Gradients of M and β

In this proof, we use the subscripts h, i, j, k to denote the element index, e.g., y_k is the k -th component of vector \mathbf{y} , $M_{i,j}$ is the element in the i -th row and j -th column of matrix M , and $M_{i,:}$ is the row vector in the i -th row of M .

Rewrite $\mathbf{y} = M^{-1}\beta$ as

$$y_k = \sum_h [M^{-1}]_{k,h} \beta_h. \quad (25)$$

Differentiate y_k with respect to β_i ,

$$\frac{\partial y_k}{\partial \beta_i} = [M^{-1}]_{k,i}. \quad (26)$$

Differentiate l with respect to β_i using the chain rule,

$$\frac{\partial \ell}{\partial \beta_i} = \sum_k \frac{\partial \ell}{\partial y_k} \frac{\partial y_k}{\partial \beta_i} = \sum_k [M^{-1}]_{k,i} \frac{\partial \ell}{\partial y_k} = [M^{-\top}]_{i,:} \frac{\partial \ell}{\partial \mathbf{y}}. \quad (27)$$

Express the derivative in vector form,

$$\frac{\partial \ell}{\partial \beta} = M^{-\top} \frac{\partial \ell}{\partial \mathbf{y}} = M^{-1} \frac{\partial \ell}{\partial \mathbf{y}}. \quad (28)$$

Differentiate y_k with respect to $M_{i,j}$,

$$\frac{\partial y_k}{\partial M_{i,j}} = \frac{\partial \left(\sum_h [M^{-1}]_{k,h} \beta_h \right)}{\partial M_{i,j}} = \sum_h \beta_h \frac{\partial [M^{-1}]_{k,h}}{\partial M_{i,j}}. \quad (29)$$

Differentiate of $[M^{-1}]_{k,h}$ with respect to $M_{i,j}$,

$$\frac{\partial [M^{-1}]_{k,h}}{\partial M_{i,j}} = -[M^{-1}]_{k,i} [M^{-1}]_{j,h}. \quad (30)$$

Substitute the derivative back into the expression,

$$\frac{\partial y_k}{\partial M_{i,j}} = -[M^{-1}]_{k,i} \sum_h [M^{-1}]_{j,h} \beta_h = -\frac{\partial y_k}{\partial \beta_i} y_j. \quad (31)$$

Differentiate l with respect to $M_{i,j}$ using the chain rule,

$$\frac{\partial \ell}{\partial M_{i,j}} = \sum_k \frac{\partial \ell}{\partial y_k} \frac{\partial y_k}{\partial M_{i,j}} = -y_j \sum_k \frac{\partial \ell}{\partial y_k} \frac{\partial y_k}{\partial \beta_i} = -y_j \frac{\partial \ell}{\partial \beta_i}. \quad (32)$$

Express the derivative in matrix form,

$$\frac{\partial \ell}{\partial M} = -\frac{\partial \ell}{\partial \beta} \mathbf{y}^\top. \quad (33)$$

Appendix B. Further Experimental Details

B.1 Standalone Validation

We list the linear ODEs used for the validation experiment and their closed-form solutions. There are five ODEs from ODEBench (d'Ascoli et al., 2024) and an additional third-order ODE. c_0, c_1, c_2 are constant numbers. $u_0 = y(0), u_1 = y'(0), u_2 = y''(0)$ are initial values.

RC-circuit (charging capacitor), $(c_0, c_1, c_2) = (0.7, 1.2, 2.31), (u_0) = (10),$

$$\frac{y}{c_1} + c_2 \frac{dy}{dt} = c_0, \quad (34)$$

$$y = c_0 c_1 + (u_0 - c_0 c_1) \exp\left(-\frac{t}{c_1 c_2}\right). \quad (35)$$

Population growth (naive), $(c_0) = (0.23), (u_0) = (4.78),$

$$c_0 y - \frac{dy}{dt} = 0, \quad (36)$$

$$y = u_0 \exp(c_0 t). \quad (37)$$

Language death model for two languages, $(c_0, c_1) = (0.32, 0.28), (u_0) = (0.14),$

$$(c_0 + c_1) y + \frac{dy}{dt} = c_0, \quad (38)$$

$$y = \frac{c_0}{c_0 + c_1} - \left(\frac{c_0}{c_0 + c_1} - u_0\right) \exp(-(c_0 + c_1)t). \quad (39)$$

Harmonic oscillator without damping, $(c_0) = (2.1), (u_0, u_1) = (0.4, -0.03),$

$$c_0 y + \frac{d^2 y}{dt^2} = 0, \quad (40)$$

$$y = u_0 \cos(t\sqrt{c_0}) + \frac{u_1}{\sqrt{c_0}} \sin(t\sqrt{c_0}). \quad (41)$$

Harmonic oscillator with damping, $(c_0, c_1) = (4.5, 0.43), (u_0, u_1) = (0.12, 0.043),$

$$c_0 y + c_1 \frac{dy}{dt} + \frac{d^2 y}{dt^2} = 0, \quad (42)$$

$$y = \exp\left(-\frac{c_1}{2}t\right) \left(u_0 \cos\left(\frac{t}{2}\sqrt{4c_0 - c_1^2}\right) + \frac{c_1 u_0 + 2u_1}{\sqrt{4c_0 - c_1^2}} \sin\left(\frac{t}{2}\sqrt{4c_0 - c_1^2}\right) \right). \quad (43)$$

Additional third-order ODE, $(u_0, u_1, u_2) = (0, -1, 1),$

$$\frac{dy}{dt} + \frac{d^2 y}{dt^2} + \frac{d^3 y}{dt^3} = 0, \quad (44)$$

$$y = u_0 + u_1 + u_2 + \exp\left(-\frac{t}{2}\right) \left(-(u_1 + u_2) \cos\left(\frac{\sqrt{3}}{2}t\right) + \frac{\sqrt{3}}{3}(u_1 - u_2) \sin\left(\frac{\sqrt{3}}{2}t\right) \right). \quad (45)$$

B.2 Lorenz Discovery

Table 3 lists the discovered coefficients after final fine-tuning, along with the results from the state-of-the-art method SINDy (Brunton et al., 2016a). Our S-MNN closely matches the ground truth, SINDy, and both the original MNN solvers, with only minor differences observed.

Table 3: Discovered coefficients for the Lorenz system using different methods.

Method	a_1	a_2	a_3	a_4	a_5	a_6	a_7
Ground Truth	-10	10	28	-1	-1	-8/3	1
SINDy	-10.000	10.000	27.998	-1.000	-1.000	-2.667	1.000
MNN Dense	-10.0003	10.0003	27.9760	-0.9934	-0.9996	-2.6660	0.9995
MNN Sparse	-10.0055	10.0061	27.7165	-0.9304	-0.9937	-2.6641	0.9990
<i>S-MNN</i>	-10.0003	10.0004	27.9915	-0.9968	-0.9997	-2.6664	1.0000